

On the bar pattern speed determination of NGC 3367

R. F. Gabbasov, P. Repetto, M. Rosado

Instituto de Astronomía, Universidad Nacional Autónoma de México (UNAM), A.P. 70-264, 04510, México D.F.

`gabbasov@astroscu.unam.mx`

ABSTRACT

An important dynamic parameter of barred galaxies is the bar pattern speed, Ω_P . Among several methods that are used for the determination of Ω_P the Tremaine-Weinberg method has the advantage of model independency and accuracy. In this work we apply the method to a simulated bar including gas dynamics and study the effect of 2D spectroscopy data quality on robustness of the method. We added a white noise and a Gaussian random field to the data and measured the corresponding errors in Ω_P . We found that a signal to noise ratio in surface density ~ 5 introduces errors of $\sim 20\%$ for the Gaussian noise, while for the white noise the corresponding errors reach $\sim 50\%$. At the same time the velocity field is less sensitive to contamination. On the basis of the performed study we applied the method to the NGC 3367 spiral galaxy using H α Fabry-Perot interferometry data. We found $\Omega_P = 43 \pm 6 \text{ km s}^{-1} \text{ kpc}^{-1}$ for this galaxy.

Subject headings: galaxies: individual (NGC 3367) — galaxies: kinematics and dynamics — methods: n-body simulations — techniques: interferometric

1. Introduction

The evolution of disk galaxies is strongly influenced by the main structures within their disks, notably spirals and bars. Bars are a fundamental component of mass distribution in spiral galaxies because they may contain a large fraction of the disk. Bar kinematics is different from the one of the axisymmetric disk, which makes the study of bar parameters important, especially the bar pattern speed (Ω_P). Bar properties are tightly related to the mass distribution of the host galaxy. The shape and structure of the bar, such as vertical bending (buckling), is believed to depend on the stage of evolution (Athanasoula 2003). Moreover, Ω_P is one of the fundamental parameters in driving the evolution of bars. Noguchi (1987) finds from numerical simulations that tidally-induced bars rotate slowly in comparison with spontaneous bars. Thus, bar pattern speed may help to discriminate between spontaneous bars and tidal bars.

One of the first methods applied to bar pattern speed determination is based on the identifi-

cation of theoretically predicted resonances (Lindblad resonances, corotation), using the rotation curve to extract the periodic motion of stars and gas (Tully 1974). Contopoulos (1980) demonstrated with orbit calculations that the corotation radius should be located at the end of a self-consistent bar. However, it was shown from a survey of early-type galaxies, that indeed the bar ends rather between the inner 4 : 1 resonance and the corotation (Elmegreen et al. 1996).

An alternative method consists of matching numerical models to the observed data (Rautiainen et al. 2005). Two other methods are based on the analysis of spiral density waves. Elmegreen et al. (1992) apply a computer algorithm to extract various types of symmetries from galaxy images, while Canzian (1993) points out the difference in the global appearance of the residual velocity field of a spiral galaxy inside and outside the corotation radius. Tremaine & Weinberg (1984) formulated a method to measure the bar pattern speed that is independent from any spiral density wave theory. The principal assumption of the method is

that the surface density of the tracer of the gravitational potential (e.g., old stars) satisfies the continuity equation, i.e., there is no significant destruction or creation of the tracer over a dynamical time. This method allows the measurement of the bar pattern speed with two observational quantities: the surface brightness of the tracer and the velocity of the tracer along the line of sight. So far the method was successfully applied to some twenty galaxies. Kent (1987) and Merrifield & Kuijken (1995) apply this method to the stellar bar component of the SB0 galaxy NGC 936. Gerssen et al. (1999) apply the Tremaine-Weinberg (TW) method to the stellar component of the galaxy NGC 4596. The same authors use the method for the galaxies NGC 271, NGC1358, ESO 281-31 and NGC 3992 (Gerssen et al. 1999). Aguerra et al. (2003) applied the method for the galaxies ESO 139-G009, IC 874, NGC 1308, NGC 1440 and NGC 3412. Debattista & Williams (2001) use the TW method for NGC 7079 and for NGC 1023 (Debattista et al. 2002).

Other authors derived the bar pattern speed applying the TW method to a gaseous tracer. Westpfahl (1998) finds the bar pattern speed for M81 employing HI as a tracer. Using CO observations, Zimmer et al. (2004) employ the method for the galaxies M51, M83 and NGC 6946. Rand & Wallin (2004) consider the galaxies NGC 1068, NGC 3627, NGC 4321 (M100), NGC 4414, NGC 4736 and NGC 4826, and measure the bar pattern speed with CO as a tracer. The application of this method to the gaseous phase is more delicate because of the assumptions of the method itself. In general, the ionized gas, the CO and HI, do not satisfy the continuity equation over an orbital period and do not trace the gravitational potential. However, assuming that the gas is continuously distributed along the pattern, and that the luminosity-weighted mean is a valuable indicator of the mean mass distribution and, neglecting the internal kinematics of H II regions, some authors successfully applied the TW method to the ionized gaseous phase. Hernandez et al. (2004) employ ionized hydrogen 2D velocity fields of four barred galaxies NGC 4321, NGC 3359, NGC 6946, NGC 2903 and also of M51 to measure the pattern speed. The same authors build numerical simulations to investigate the possibility of using the gaseous component and present an application

for NGC 4321 galaxy (Hernandez et al. 2005). Emsellem et al. (2006) have successfully applied TW method for bar pattern speed determination of NGC 1068 using Fabry-Perot H α map, and also reproduce with Nbody+SPH models a number of its observed properties. Fathi et al. (2007) also with two dimensional ionized hydrogen kinematics determine the bar pattern speed of NGC 6946. Beckman et al. (2007) apply the method to a sample of nine galaxies (NGC 3049, NGC 4294, NGC4519, NGC 5371, NGC 5921, NGC 5964, NGC 6946, NGC 7479, NGC 7741) using ionized hydrogen 2D kinematic data.

In this article we employ the TW method to study the errors in the parameters that may affect the pattern speed determination. We test to which parameters the method is sensitive with numerical simulations and apply this method to the barred galaxy NGC 3367.

2. Numerical test of the TW method

The Tremaine Weinberg method uses two observable quantities: the luminosity weighted velocity and luminosity weighted density determined along a thin strip (aperture) parallel to the major axis of the disk (Tremaine & Weinberg 1984). If a galaxy is centered at the cartesian coordinates such that the major and minor axes are aligned parallel to the x and y axes, respectively, then the ratio of intensity-weighted velocity and intensity-weighted position gives the angular velocity:

$$\Omega_P \sin i = \frac{\langle V(x) \rangle - V_{sys}}{\langle x \rangle - x_0}. \quad (1)$$

Here V_{sys} is the systemic velocity, and x_0 is the position of the kinematic center of the disk along x axis. The Ω_P is also corrected due to inclination i ($i = 0$ corresponds to face-on disk). This formulation of Merrifield & Kuijken (1995) allows a more accurate evaluation of Ω_P because the errors in the dynamical center and systemic velocity determination are reduced. Thus, estimating the above expression for several apertures, one may plot $\langle V \rangle$ vs. $\langle x \rangle$ and obtain the averaged value of Ω_P .

One of the conditions required by the TW method is that the tracer should satisfy the continuity equation. The old stars in SB0 galaxies, for example, survive long enough to trace the spiral pattern potential. The main concern regarding

the validity of application of the TW method to gaseous tracer is that the ISM, composed mostly of molecular and atomic hydrogen, is not able to trace the potential for a long period of time due to short timescale processes such as phase transitions, cooling, etc. Nevertheless, it was successfully applied to CO emission lines (Rand & Wallin 2004; Zimmer et al. 2004) and to the H α emission line (Hernandez et al. 2005; Emsellem et al. 2006; Fathi et al. 2007). As was shown by Westpfahl (1998) addition or subtraction of the tracer material has no effect on calculation of the instantaneous pattern speed, and thus, it is expected that processes of star formation and feedback may be neglected. Hernandez et al. (2005) have demonstrated by hydrodynamical simulations that the application of the method to ionized gaseous phase is reliable under some assumptions. The problem arises rather in the quality of the image and the velocity field as affected by regions of star formations, dust obscuration, and local gas motions. An argument in favor of applicability of the method is that the H α image also contains the stellar continuum emission. This should alleviate the problem of a patchy monochromatic image, making it smoother. All these arguments are still have to be carefully verified, and here we assume as a working hypothesis that application of the TW method to the H α kinematic data is valid.

As it was shown by Debattista (2003) the method is very sensitive to errors in the determination of the position angle (PA) of the major axis. On the other hand, as shown by Rand & Wallin (2004), the molecular gaseous component may produce a non-zero pattern speed even in the absence of any clear wave pattern due to clumpiness. The latter point requires that the determination of Ω_P should be done with much caution. In particular, Hernandez et al. (2005) have shown by means of hydrodynamical simulations that the regions of shocks and the zones outside the bar should be avoided. The effects of the inclination, bar orientation, angular resolution, and the uncertainty were already investigated in numerical models by Rand & Wallin (2004).

2.1. Numerical models

In order to test the influence of errors in intensity and 2D velocity fields on the determination of the pattern speed with the TW method we per-

formed numerical simulations of a bar formed in a hydrodynamic (Nbody+SPH) and collisionless (Nbody) disk galaxy.

For this purpose we prepared a bar unstable disk galaxy consisting of total 3×10^6 particles sampling an exponential stellar and gas disks, and a Hernquist halo (Hernquist 1990). The vertical structure of the disk is described by isothermal sheets with a constant scale height of 280 pc for stars and 80 pc for gas. Gas dynamics obeys the isothermal equation of state with a temperature $T = 10^4$ K. The processes of star formation and feedback were not included. The model was constructed using a technique similar to that described by Hernquist (1993) and the numerical parameters were chosen according to Gabbasov et al. (2006). The galaxy model parameters are summarized in the Table 1. The simulation was performed with GADGET 2 code on HP CP 4000 cluster (KanBalam) at DGSCA-UNAM.

We estimate the bar pattern speed as follows. At each snapshot we determine the orientation of the principal axes of the inertia tensor of the bar. Then, we draw the bar position angle as a function of time, and the Ω_P is obtained by numerical differentiation, $\Omega_P = d\phi/dt$. The bar appears at a time $t \sim 2$ Gyrs and at $t = 3$ Gyrs reaches its maximum length of ~ 7 kpc. For $t = 4$ Gyrs most of the gas is transferred to the center of the disk. During this period, the angular velocity of the bar remains roughly constant, 41 km s^{-1} . Further evolution leads to the depletion of the gas particles along the bar, and after about 5 Gyrs, the gas is rather located in the center and in the spiral arms. For our analysis we took the snapshot at $t = 3.75$ Gyrs when the bar is oriented $\sim 40^\circ$ from the vertical y axis. We added some systemic velocity to the velocity field and inclined the disk by $i = 30^\circ$,

Table 1: Galaxy model parameters.

Parameter	Gas	Disk	Halo
M ($10^{10} M_\odot$)	0.4	3.96	22
r_0 (kpc)	3.3	3.3	6.6
N (10^6)	0.2	0.8	2.0
ε (pc)	80	80	160

NOTE.—Here M is the mass of the component, r_0 - the scale radius, N - the num

such that the disk major axis is aligned with the x axis. We compute the projected on the sky plane 2D surface density and the velocity fields on uniform cartesian grids of 204×204 , see Fig. 1. We apply the TW method to simulated stellar and gas bars and compared Ω_P with the pattern speed obtained from the simulation. A difference of less than 1.0 km s^{-1} was found for the stellar bar. The gas pattern speed was overestimated by $\sim 7 \text{ km s}^{-1}$, because of the surface density weighting errors. We also applied the method to the galaxy at $t = 1 \text{ Gyrs}$ (early stage of evolution without a bar) and obtained a zero slope as expected.

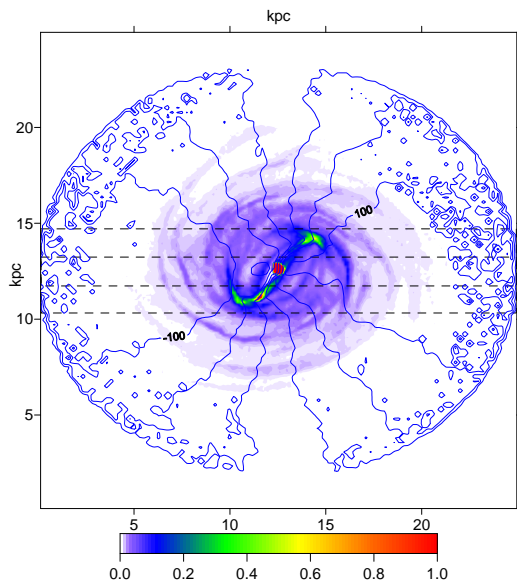


Fig. 1.— Projected surface density of the gas, with the corresponding velocity contours overlaid. The surface density is normalized by the maximum value. The contours are separated by 40 km s^{-1} and dashed lines show some of the slit positions (one of ten).

2.2. PA variation

First, we tested the sensitivity of the bar pattern speed to variations of the position of the major axis of the simulated disk galaxy, which could be interpreted as errors in the determination of PA. Here, the variation in the position angle δPA , is the angle between the disk major axis and the x axis of the fixed reference frame. The resulting Ω_P is presented in Fig. 2. For the considered range

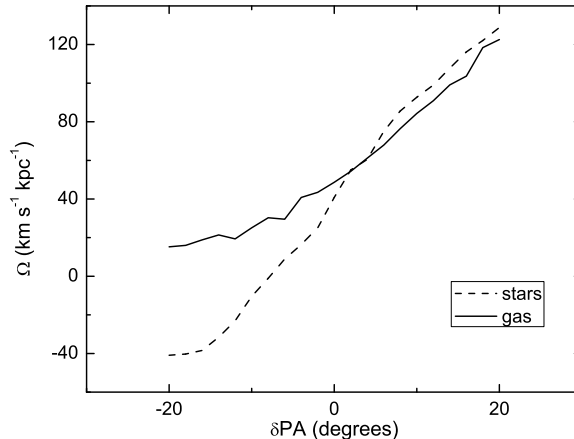


Fig. 2.— Dependence of Ω_P on the PA variation.

of δPA and bar orientation the Ω_P changes almost linearly. As the bar tends to become aligned with the y axis the pattern speed reduces. From this plot one may observe that an uncertainty of $\delta\text{PA} \pm 5^\circ$ gives rise to an error in Ω_P of $\pm 15 \text{ km s}^{-1} \text{ kpc}^{-1}$ for gas bar.

As an example, in Fig. 3 we plot the $\langle x \rangle$, $\langle V \rangle$, and in Fig. 4 the normalized mean surface density $\langle \Sigma \rangle / \Sigma_{MAX}$ vs. y for 40 apertures of width 0.12 kpc about the kinematic center located at $y_0 = 2.45 \text{ kpc}$. Also in Fig. 4 shown is the resulting $\langle V \rangle$ to $\langle x \rangle$ ratio. In order to avoid a discontinuity in center of these plots we have excluded from the analysis the central four pixels with very high gas density. The plots are shown for $\delta\text{PA} = 0, -10^\circ, +10^\circ$ (solid, dotted, and dashed line, respectively).

As seen from Fig. 3, the weighted average velocity is the most sensitive quantity in the plot, and the difference comes mainly from the ends of the bar, while at the center the slope varies slowly for all three cases. At the same time the slope of $\langle x \rangle$ changes in opposite direction than $\langle V \rangle$, affecting strongly the Ω_P determined. The decaying intensity and velocity profiles in the first and the last kiloparsec are due to inclusion of the apertures containing spiral arms at the ends of the bar. This is observed as a characteristic \mathcal{Z} -shape, or a loop-shape, in the $\langle V \rangle$ vs. $\langle x \rangle$ plot in Fig. 4, instead of a straight line. The weighted averaged intensity also changes the position and the maximum of its shoulders, being nearer to the center and

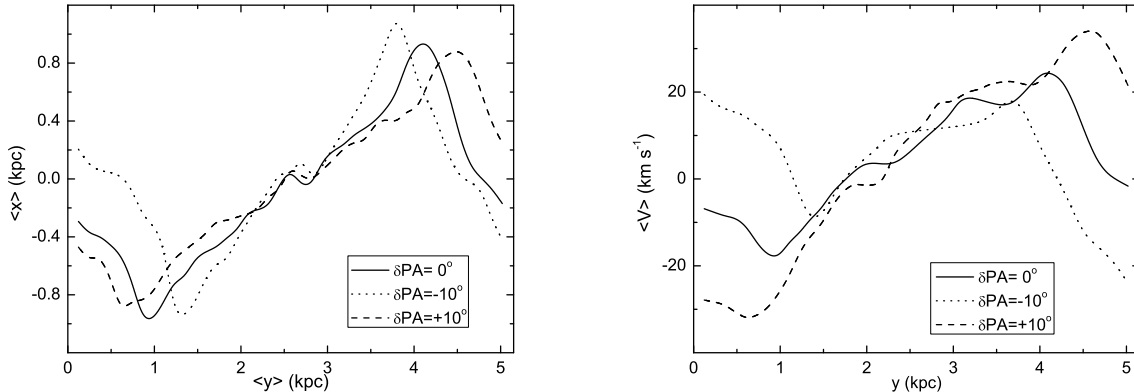


Fig. 3.— Dependence of $\langle X \rangle$ and $\langle V \rangle$ on PA variation.

higher for closer alignment of the bar with the y axis. Unfortunately, the restriction in y does not reduce significantly the errors produced by variation of PA.

2.3. Disk thickness

According to the original formulation of the method, it is valid only for an infinitely thin disk. However, galactic disks generally have a certain thickness and line of sight velocities also contain the projected component of velocity normal to the disk (Z component, $v_z \cos i$). This component becomes important as the inclination approaches 0 degrees, i.e., the galaxy becomes face on. For a disk symmetric in the Z direction the vertical motions cancel out each other, and the net contribution is zero. However, the presence of an asymmetry in vertical structure (such as bar buckling) will also introduce asymmetry in the velocity field. We have verified this argument by including the projected Z component of velocity in a simulated bar velocity field. For our Nbody+SPH model, evolved for 5 Gyrs, we found no significant difference in Ω_P for both gas and stellar bars. We also prepared and ran a pure collisionless model, incrementing the stellar disk mass by the mass of removed gas disk. We traced the evolution of the bar up to 10 Gyrs, and quantify the bar buckling as a change of r.m.s. of the vertical velocity dispersion of disk particles, σ_z . Due to heating of the stellar disk the vertical dispersions grow linearly until the bar begins to buckle at $t \approx 4.5$ Gyrs. After the buckling, the r.m.s. dispersions are rapidly increased by $\sim 10\%$ and this is reflected in a reduc-

tion of the pattern speed slowdown rate, as shown in Fig. 5. The determination of the pattern speed becomes more robust as the spiral arms cease, and the curve that does not include the Z component is much smoother, except for some spikes. In contrast, inclusion of the Z component clearly affects the instantaneous Ω_P determination due to buckling, but the errors are quite small (a few km s^{-1}). Thus, for old stellar bars, where buckling is strong and the velocity dispersions are high, the vertical motions could make an important contribution to the observed velocity field introducing errors in the Ω_P determination by the TW method.

2.4. Data quality

Next, we checked the robustness of the TW method to the introduction of an artificial noise to the surface density and velocity fields. Such noise is naturally present in the observed data. First, we add a white noise background to our simulated surface density field to represent the emission inhomogeneities. The white noise background was created by assigning to each pixel a random value within $(0, \Sigma_{\text{pert}})$ in case of intensity field and $(-V_{\text{pert}}, +V_{\text{pert}})$ in case of velocity field. Here, Σ_{pert} and V_{pert} are the maximum values of perturbation of the surface density and velocity field, respectively. The results are shown in Fig. 6. As we increment the amplitude of the perturbation relative to the corresponding maximum value of the surface density ($\Sigma_{\text{pert}}/\Sigma_{\text{max}}$) or the velocity field ($|V_{\text{pert}}|/|V_{\text{max}}|$), the errors become dominant. Indeed, for the ratio $\Sigma_{\text{pert}}/\Sigma_{\text{max}} > 0.3$ (signal to noise ratio < 5) for white noise, the

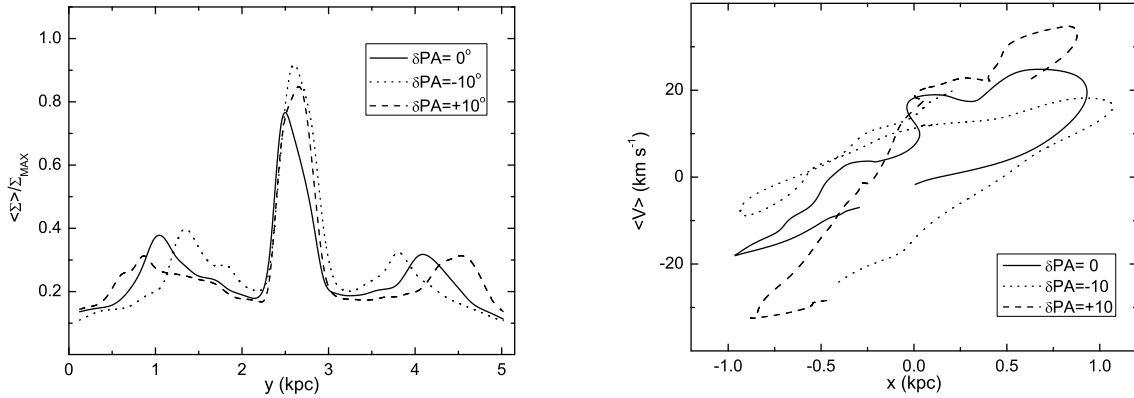


Fig. 4.— Dependence of $\langle \Sigma \rangle$ and the slope $\langle V \rangle$ vs. $\langle x \rangle$ on PA variation.

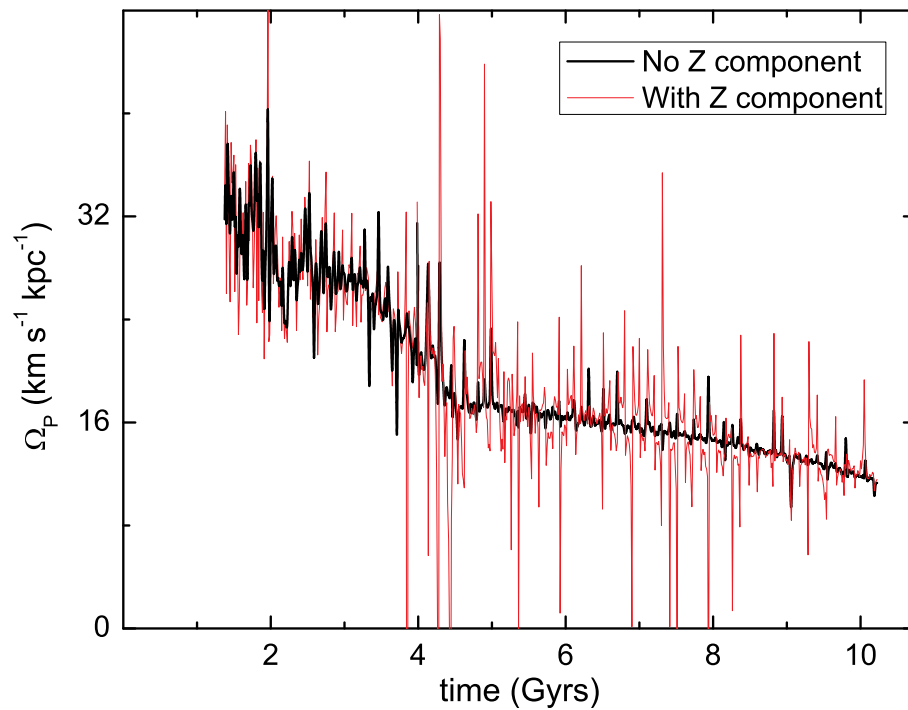


Fig. 5.— Pattern speed of a collisionless bar determined with TW method, including and excluding the Z component (red thin and black thick curve, respectively).

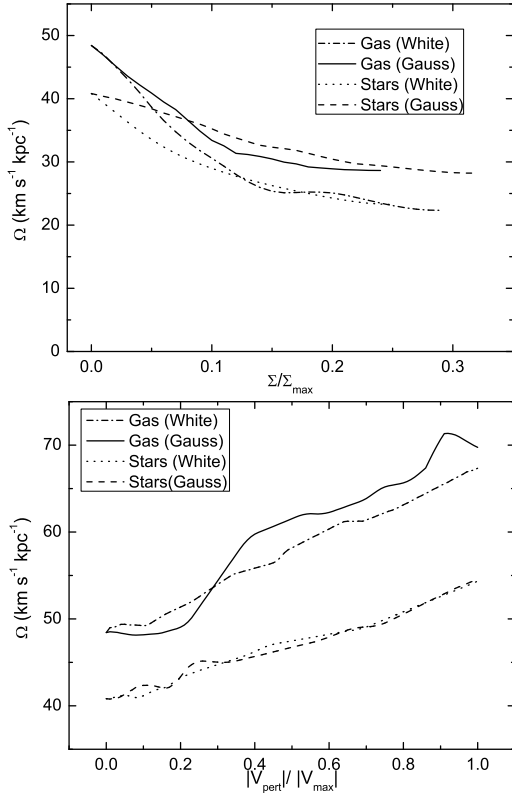


Fig. 6.— Variation of Ω_P with the degree of contamination of intensity (top) and velocity (bottom).

determination of the pattern speed is not possible anymore because a clear slope cannot be established. As a next step, we test the sensitivity of the method to the Gaussian noise. Besides the observational noise it simulates local gas inhomogeneities in the disk. We create a random Gaussian field with spherical ($\theta = 10$) correlation function and also change its amplitude relative to the maximum value of the signal (see Fig. 7). For this purpose, we used the software developed by Kozintsev & Kedem (2000). When added to the intensity field, the signal is also underestimated, although not so strongly as in the case of white noise. Concerning the velocity field contamination, one can note that the determination of the Ω_P is possible, even reaching the ratio $|V_{\text{pert}}|/|V_{\text{max}}| \sim 1$. However, in the case of the Gaussian random field the errors influence stronger the resulting $\langle V \rangle$ vs. $\langle x \rangle$ slope for the gas bar. Note, that the pattern speed is either underestimated or overestimated for different bar positions and, in case of the Gaussian noise, for different realizations of the field.

In addition, we investigate the effect of a clipping procedure (i.e., imposing the inferior limit on the surface density) and finding that the effect on the resulting pattern speed has rather non-linear trend as can be seen in Fig. 8. The surface densities of both stellar and gas components were normalized by their respective maximum values. The most sensitive part of the curve is due to clipping of up to a few percent of the maximum surface density, which corresponds to the density of the faint spiral arms and the disk that leads to an overestimation by more than 50% in the pattern speed (cf. surface density distribution in Fig. 1 and Fig. 4). A roughly flat region of the curves where the bar size due to successive clipping diminishes and becomes thinner, the Ω_P of both gas and stellar bar is reaching $65 \text{ km s}^{-1} \text{kpc}^{-1}$. A rapid drop in the curves corresponds to the clipping when the bar is not continuous anymore, but rather looks like two bright patches, after which the determination of the pattern speed is barely possible. This behavior holds for several snapshots we have analyzed between 2 and 4 Gyrs of evolution. The same mechanism should be responsible for a rapid change in Ω_P for small Σ_{pert} values added to the intensity field. Perturbations of the surface density of the the same amplitude as of the faint disk

and spiral arms lead to underestimation as shown in Fig. 6. Thus, we may conclude that the role of the spiral arms in the application of the TW method is very important. A similar conclusion was reached by Rand & Wallin (2004) who found that too much clipping could violate the principal assumption of the TW method and lead to incorrect pattern speed determinations. On the other hand, we found that the restriction of the maximum surface density (clipping “from above”) produces the bifurcation in the center of $\langle V \rangle$ vs. $\langle x \rangle$ plot (not shown here), creating an effect of presence of two different pattern speeds. The size of the bifurcated area increases with the diminishing of the upper limit of the surface density. If these points are omitted from the linear fit, the resulting pattern speed is not affected.

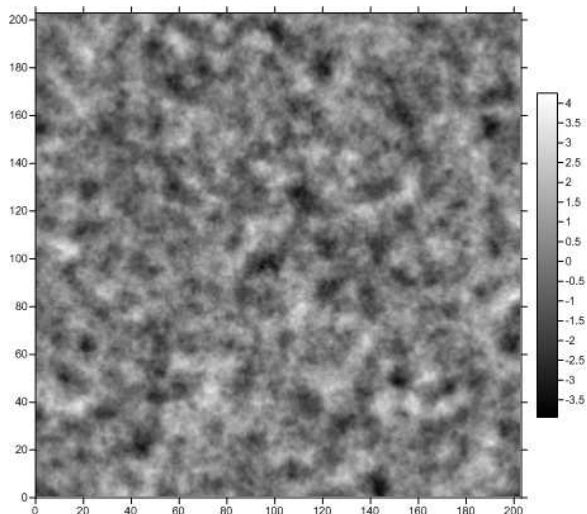


Fig. 7.— Random Gauss field used for data quality study.

The observations measure the intensity of H α emission line rather than the gas surface density. The results above were analyzed only for the surface density field of gas and stars derived directly from the simulation, but not for the intensity field produced by ionized gas. The original TW method is formulated for the stellar component, where it is assumed that the disk surface density is directly proportional to the number of stars per unit area. However, in the case of the gas, the tracer is sensitive to the square of the density because the regions of ionized hydrogen will produce recombin-

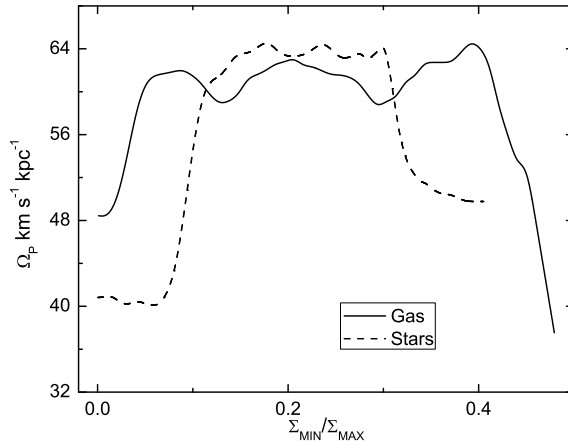


Fig. 8.— Variation of Ω_P with the degree of clipping of the surface density.

tion lines whose rough emissivity is given by

$$I \sim \rho^2 T^{-1/2} \quad (2)$$

If we assume that the gas is isothermal everywhere in the disk, then the emission map will be a function of gas density squared only. In this case, our simulations show that Ω_P is overestimated by roughly 30%. Nonetheless, when the emission map is clipped at the bar level (i.e., masking the spiral arms and disk) the value of Ω_P is not changed. The same result was found for the the observed H α emission map, presented in the next section, if transformed into the surface density of the gas. The clipping is important in this case because the transformation given by equation 2 mainly affects the regions with high density gradients, i.e., transitions between bar and disk.

These results establish the validity margins of the TW method for our models. Although they were determined for a simple galaxy model, they give us the general clues on parameter dependencies. Complete hydrodynamical simulations, including star formation, supernovae feedback and radiative cooling will be presented elsewhere.

3. Application to NGC 3367

NGC 3367 is classified as a SBc type barred galaxy and it is considered as an isolated galaxy at a distance of 43.6 Mpc ($H_0 = 75 \text{ km s}^{-1} \text{ Mpc}^{-1}$), located behind the Leo Spur group of galaxies. This galaxy has a remote neigh-

bor, NGC 3419, at a distance of 900 ± 100 kpc (García-Barreto & Rosado 2001). At a radius of 10 kpc from the nucleus there is an optical structure consisting of several $H\alpha$ knots that resembles a bow-shock (García-Barreto et al. 1996a,b). García-Barreto et al. (1998) report Very Large Array (VLA) observations with an angular resolution of $4.5''$ at 1.46 GHz and find radio continuum emission from two lobes that extend up to 6 kpc outside the plane of the disk, and a weaker emission from the same disk. Gioia et al. (1990) also reported soft X-ray emission from this galaxy.

3.1. Ionized hydrogen kinematics data analysis

We use the ionized hydrogen data cube from Fabry-Perot interferometry observations published in García-Barreto & Rosado (2001). The data cube has dimensions $512 \times 512 \times 48$, a final image scale of $0.58'' \text{ pixel}^{-1}$, and spectral sampling of 19 km s^{-1} . García-Barreto & Rosado (2001) used an interference filter with a central wavelength of 6620\AA , and a narrow band (30\AA) in order to isolate the redshifted $H\alpha$ emission of this galaxy. The authors made the calibration with a neon lamp centered at 6598.95\AA . The exposition time for each channel was of 120 s. No attempt was made by the authors for absolute calibration of the $H\alpha$ emission.

The data were already reduced with the AD-HOCw¹ software, and we use it to obtain the intensity $H\alpha$ monochromatic map, the radial velocity field, and the continuum map. The $H\alpha$ image we use for our further analysis was obtained by sum of 20 channels, without subtraction of the continuum. The velocity field was obtained by finding the barycenter of the $H\alpha$ profile peaks for each pixel. The photometric center was determined from the continuum map by looking for the brightest pixel, which in this case coincides with the kinematic center (Fuentes-Carrera et al. 2004, 2007). We trimmed these maps to 204×204 to exclude external sources and employ a spectral and spatial smoothing with a Lorentzian function with a FWHM of 3 pixels ($\sim 1.7''$ compared with the seeing $\sim 1.2''$), more adapted to the instrumental function of a Fabry-Perot. The final $H\alpha$ image

and the radial velocity field are shown in (Fig. 9).

We use the two dimensional radial velocity field to obtain a rotation curve for NGC 3367. García-Barreto & Rosado (2001) already obtained a rotation curve for this galaxy using the AIPS package. For this work we wish to explore the variation of the parameters of the rotation curve in order to optimize them because they are of fundamental importance for determining the bar pattern velocity. For this purpose we use the AD-HOCw software. These parameters are: inclination i , position angle PA of the major kinematic axis, systemic velocity V_{syst} and kinematic center. We obtain values similar to those published in García-Barreto & Rosado (2001) with the difference that our systemic velocity and position angle are slightly higher: $V_{syst} = 3164 \pm 10 \text{ km s}^{-1}$ instead of $V_{syst} = 3030 \pm 8 \text{ km s}^{-1}$, $PA = 60^\circ \pm 5^\circ$ instead of $PA = 51^\circ \pm 3^\circ$. Our kinematic center is located at R.A. = $10^h 46^m 35^s$ and Dec. = $13^\circ 45' 00''$ (J2000.0), which are the same values reported by García-Barreto & Rosado (2001). The inclination with respect to the plane of the sky is $i = 30^\circ \pm 5^\circ$ as in García-Barreto & Rosado (2001). As reported by García-Barreto et al. (2007) the stellar bar length is $32''$ (6.7 kpc) and is oriented $15^\circ \pm 5^\circ$ from the kinematic major axis.

The rotation curve was determined by averaging velocities in two sectors along the kinematic line of nodes. Once obtaining the full rotation curve of NGC 3367, we average the rotation curve over both sectors. We fit the mean rotation curve using a weighted asymptotic regression model. The rotation curve of NGC 3367, the averaged rotation curve and the fit are shown in Fig. 10.

4. Application of the TW method to NGC 3367

We apply the Tremaine-Weinberg method to NGC 3367 in order to measure the bar pattern speed. We built an IDL program that calculates the intensity-weighted velocity $\langle V \rangle$ and the intensity-weighted position $\langle x \rangle$ for each strip along the kinematic minor axis of the galaxy. Here the $H\alpha$ intensity serves as a weighting function under the assumption that the surface density of the disk is proportional to the $H\alpha$ intensity ($\Sigma_{disk} \propto I_{H\alpha}$).

The TW method involves many parameters among which we consider the position angle of

¹<http://www.oamp.fr/adhoc/adhocw.html> developed by J. Boulesteix.

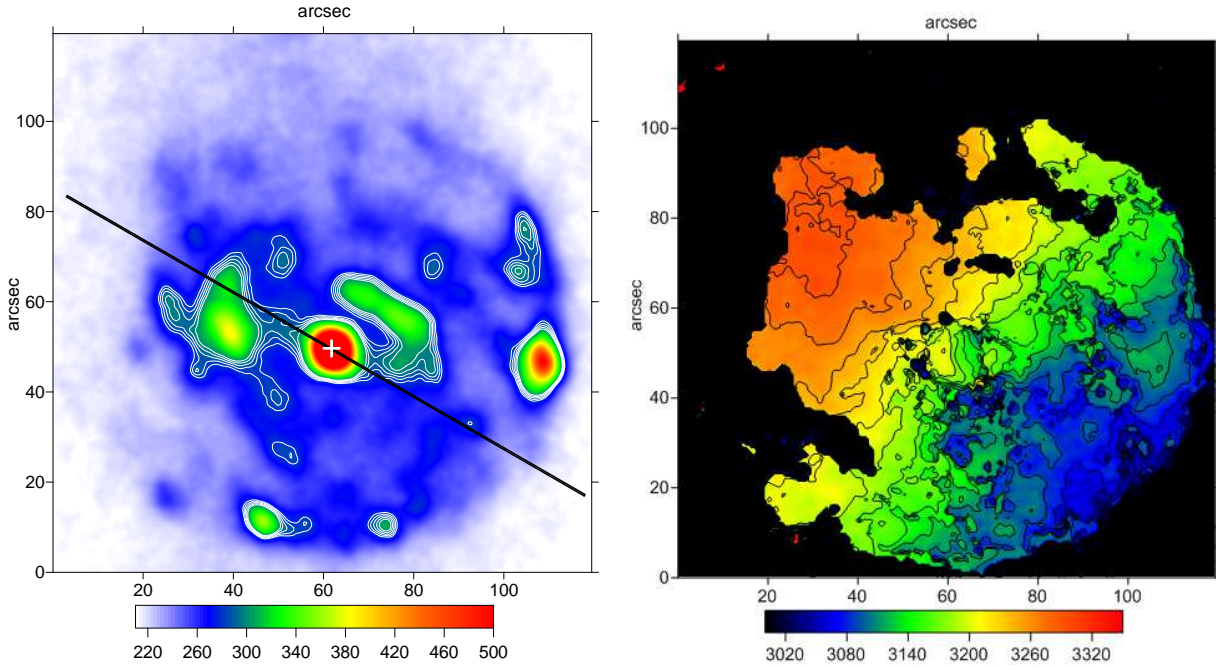


Fig. 9.— $H\alpha$ image (left) and radial velocity field of NGC 3367 with contours levels separated by 20 km s^{-1} (right). The contours on the $H\alpha$ image depict the bar region and are shown from 280 to 300 with step of 5 in arbitrary units. Also shown on the left panel is the position of the major axis and the photometric center. The north direction is on top and the east is on the left.

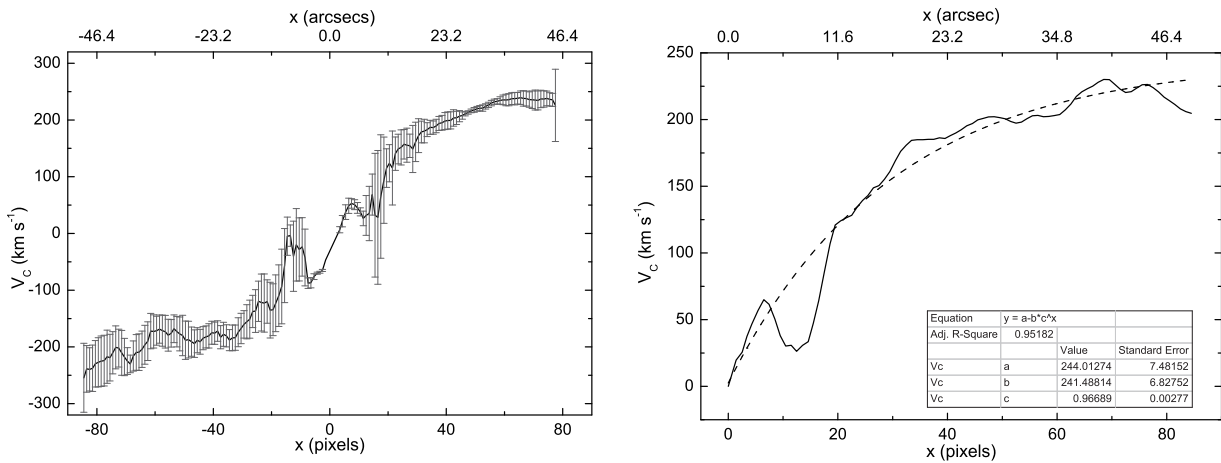


Fig. 10.— Full rotation curve of NGC 3367 (left panel) and averaged rotation curve (right panel, solid line) with overplotted fit (dashed line). See the text for further details.

the kinematic major axis (PA), the minimum and maximum of the surface brightness image, position of the kinematic center in pixels, systemic velocity, inclination, the range of integration along the major axis and the location and number of apertures along which we calculate the quantities $\langle V \rangle$ and $\langle x \rangle$. In order to explore the errors in the Ω_P determination associated with the uncertainties in the parameters we vary each of them to build a range of values. We assume that within each determined interval there is a subset of values where Ω_P is trustworthy if the plots of the weighted mean velocity and position show little scatter such that the slope in the $\langle V \rangle$ vs. $\langle x \rangle$ plot is well fitted and passes through the origin. On the other hand, in our case the curves of intensity-weighted velocity and position should start from negative values and move smoothly towards positive ones. By varying the full set of parameters we found that four of them are actually relevant. These are the PA, the minimum of the H_α image, the length of the slit along the kinematical major axis and the range of variation along the minor axis of the galaxy. The errors in V_{sys} , and kinematic center have smaller effect on Ω_P , as was already noted by Merrifield & Kuijken (1995).

Thus, we begin with the variation of PA. We establish the origin of the Cartesian coordinate system on the photometric center of the H_α image of NGC 3367, such that the x axis is aligned with the disk kinematic major axis. First, we vary the PA within the range of errors determined from the ADHOCw package ($\pm 5^\circ$) in both north-east direction (positive) and in the south-east direction (negative). From Fig. 11 it can be noted that a variation of δPA by $\pm 5^\circ$ leads to errors in Ω_P of $\pm 6 \text{ km s}^{-1}$. We extend this range up to 19° in order to compare it with the behavior of Ω_P observed in the simulation. The result presented in Fig. 11 shows that for $\delta PA > 0$ the curve is almost linear and roughly similar to the Fig. 2. As the bar becomes aligned with the kinematic major axis ($\delta PA < 0$), the Ω_P approaches zero faster. A similar conduct is found for the simulated bar oriented in the same way as the observed one ($\sim 15^\circ$ from the major axis).

In order to select only those emission regions near the bar, we mask the H_α image by changing the minimum of the image. Clipping to a given minimum H_α intensity is necessary because

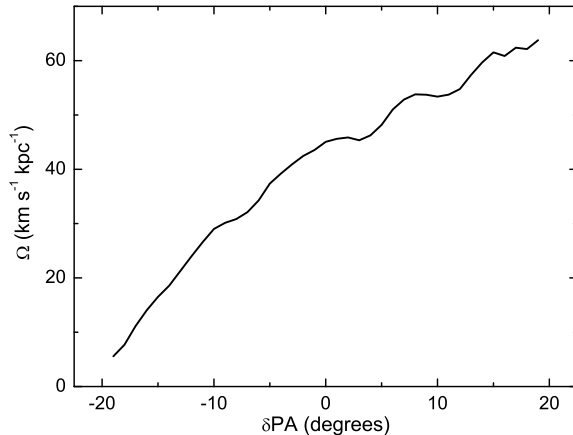


Fig. 11.— Variation of Ω_P with position angle of the disk of NGC 3367.

if the entire image is taken the plot of $\langle V \rangle$ vs. $\langle x \rangle$ is too noisy and it is difficult to establish a clear fit. As shown in the previous section a sufficiently noisy background could strongly affect the results. The masking procedure helps to hide bright knots within the interarm regions and allows to achieve higher signal to noise ratio. Additionally, as demonstrated by Rand & Wallin (2004), intensity clipping helps to improve the results by removing the scatter produced by clumps, but at the same time it could also remove part of the bar pattern. Fig. 12 shows the variation of Ω_P with the minimum of the H_α image. The range of varied intensity corresponds to emission that roughly traces disk, spiral arms, and the bar region, except the bright bulge. When compared with the Fig. 8 a similar behavior of the pattern speed due to clipping can be observed. Within the bar region (excluding disk and arms) the errors due to clipping are $\pm 5\%$. The small variation of Ω_P within the clipping range 210 – 240 is probably due to the clumpiness of the H_α image around the bar. We also examined the clipping of the maximum intensity and found that it did not significantly alter the results.

Strong emission along the spiral arms represent a great source of noise in bar pattern speed determination that one needs to isolate in order to correctly perform the weighting procedure. The emission intensity of spiral arms is much stronger than that of the bar, and $\langle x \rangle$ and $\langle V \rangle$ will be biased by the arms. For this reason we resort to con-

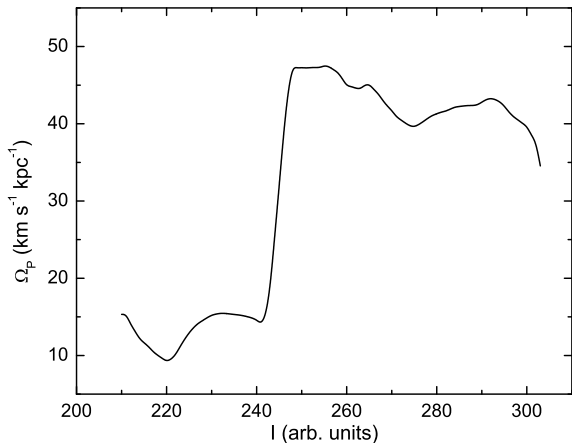


Fig. 12.— Variation of Ω_P with the minimum of intensity of the H_α image.

straining the integration area uniquely to the bar zone. We restrict the range of integration along the kinematical major axis to avoid the region of the eastern arm. This is an extended and prominent zone that biases significantly the signal to noise ratio of the intensity near the north-east side of the bar (Fig. 9). Since we are interested in the bar pattern speed, avoiding spiral arms that may have a pattern speed distinct from that of the bar would also improve the signal. The fourth important parameter is the range along the minor axis of the galaxy, i.e., the number of apertures. If this range is not limited, the bright spiral arms of the galaxy, in particular the one located at north-west, enter in the computation and the bar pattern speed cannot be determined.

After analyzing the parameter variation we determine the bar pattern speed of NGC 3367. The parameters mentioned above were constrained in the following sequence: limiting the integration area, limiting the intensity, and varying the PA. The final masked H_α image and the region where the Ω_P was determined is shown in Fig. 13. The averaging of quantities in equation (1) is done along strips of one pixel width, totalling 18 slits parallel to the kinematic major axis within the box.

We find for NGC 3367 a value of $\Omega_P = 43 \pm 6$ km s⁻¹ kpc⁻¹. This value is consistent with the value reported in García-Barreto & Rosado (2001). In Fig. 14 we show the mean weighted position and the mean weighted velocity as a function of the

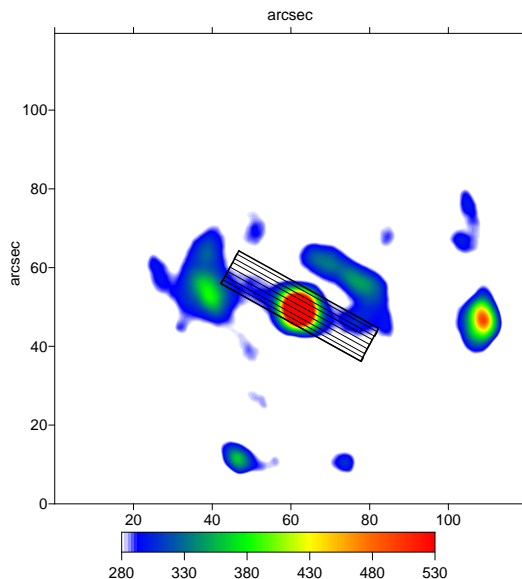


Fig. 13.— Masked H_α image and the area of integration used for the final Ω_P calculation. Some of the apertures used in the TW method were also marked. Box units are in arcseconds, and intensity is in arbitrary units.

position along the minor axis of the galaxy. Both curves show an almost linear trend, except that $\langle x \rangle$ shows flattening after $y = 11$ pixels (1.35 kpc). This is probably due to a characteristic shape of the bar, both parts of which are not symmetric and which appears to be “broken”. This asymmetry is also observed in broadband ultraviolet images (García-Barreto et al. 2007). In Fig. 15 we show the mean weighted velocity as a function of the mean weighted position and the mean intensity as a function of the position along the minor axis. The mean intensity has a bell shape similar to what is observed for a simulated bar. The sequencing of points also checks that we really measure the bar pattern speed. It is worth noting that if a linear fit is applied to the plots in Fig. 14 and then the slope is estimated, the pattern speed is $\Omega_P \approx 47$ km s⁻¹ kpc⁻¹.

4.1. Determination of Ω_P by resonances analysis.

We compared Ω_P obtained from the TW method with the one obtained from analyzing fundamental resonances of NGC 3367 predicted

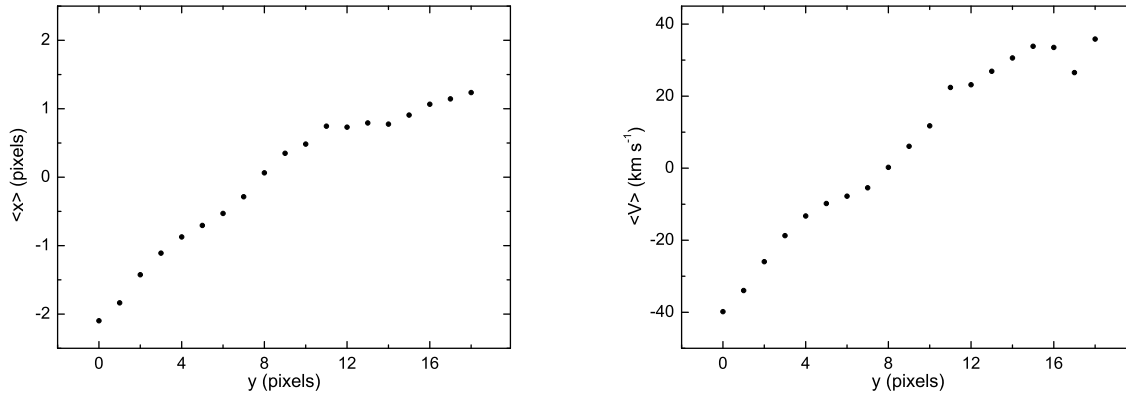


Fig. 14.— Weighted average position (left) and weighted average velocity (right) along the minor axis.

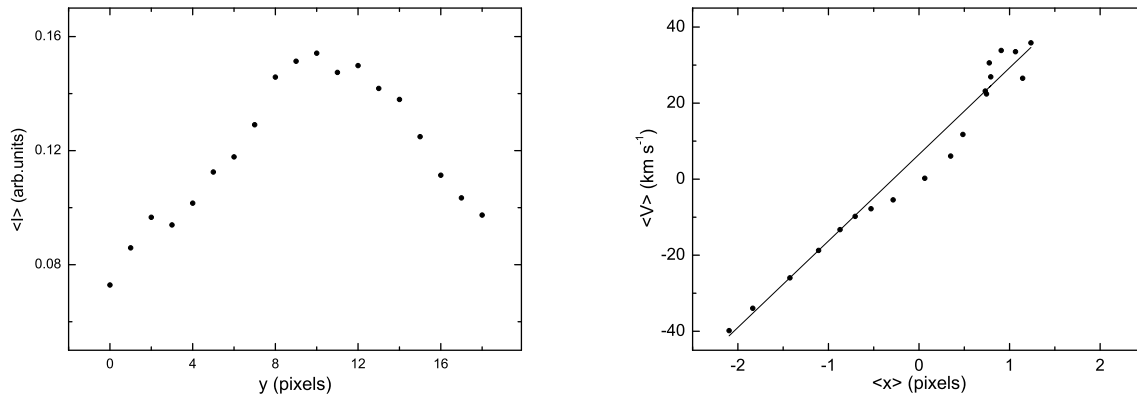


Fig. 15.— Mean intensity along the slits (left) and weighted average velocity as a function of the weighted average position (right).

by the linear theory. According to the linear theory at the resonance radii there are expected rings of matter with enhanced star formation caused by gas shocks. In particular, NGC 3367 has a ring of radius ~ 7 kpc formed by spiral arms wrapped by more than 180° . Using the diameter of the stellar bar 6.7 kpc given by García-Barreto et al. (2007) and assumption that the bar ends near the corotation, we find that $\Omega_P = 45 \pm 7 \text{ km s}^{-1} \text{ kpc}^{-1}$. Here, the errors in Ω_P are due to the rotation curve determination and fitting procedure. This value agrees within the error limits with the value we found by the TW method and also accords with the value reported in García-Barreto & Rosado (2001) of $\Omega_P = 43 \text{ km s}^{-1} \text{ kpc}^{-1}$. In Fig. 16 are shown the resonances for NGC 3367 and the bar pattern speed determined by the TW method. The resonances were obtained from the fit to the rotation curve (Fig. 10) given in this work. According to the figure the outer 4:1 resonance is located at 7.7 kpc ($36.7''$), the OLR is at some 11 kpc ($52''$), and there is no ILR. However, it should be noted that the resulting Ω_P derived in this way should be taken with caution because the ring is not necessarily located at corotation. On the other hand, given the complex structure of the rotation curve in the center and limited resolution, it is difficult to judge whether an ILR is absent or present.

5. Discussion

The main aim of this work is to estimate the bar pattern speed of NGC 3367 galaxy using $\text{H}\alpha$ kinematic data. For this purpose we first investigate the sensitivity of results to the data quality on numerical galaxy models. We have not intended to create an exact numerical model of NGC 3367, but rather to use the simulations as toy models. For this reason we cannot directly compare the lengths and pattern speeds of simulated and observed bars. We have tested the TW method for a simulated galaxy bar against contamination of surface density and velocity fields by white noise and Gaussian random field perturbations in our simulated data. We found that the surface density is critical to noise and the bar area should have a good signal to noise ratio in order to obtain reliable results, because it is used as a weighting function in equation (1). In contrast, the velocity field appears to be less sensitive to errors,

although they also affect the accuracy of the results. This is due to the zero net velocity perturbation introduced in calculus of $\langle V \rangle$ where the errors are partially cancelled out. However, for gas-poor, old stellar bars, where the buckling is significant, v_z component of the velocity field may be important. We also checked the influence of the position angle on the resulting Ω_P . In agreement with Debattista (2003) the results are sensitive to PA uncertainties. When the disk major axis and the bar become aligned, the errors in Ω_P increase faster than in the opposite case.

Based on the results of the robustness test, we apply the TW method to NGC 3367 using published 2D data of Fabry-Perot interferometry. After carefully studying the parameters that could affect the results (minimum intensity, range of integration, number of strips, high intensity knots and arms, position of kinematic major axis), we found $\Omega_P = 43 \pm 6 \text{ km s}^{-1} \text{ kpc}^{-1}$. We also determine the bar pattern speed by means of resonances analysis and found $\Omega_P = 45 \pm 7 \text{ km s}^{-1} \text{ kpc}^{-1}$. These two results are consistent and in agreement with the value reported previously by García-Barreto & Rosado (2001). The trend in variation of Ω_P with the position angle of the kinematical major axis is consistent with the result encountered in the simulated barred galaxy.

As shown in Sect. 2 the variation of the minimum of the surface density for the simulated barred galaxy could significantly affect Ω_P determination. As we have demonstrated, for NGC 3367 the adopted minimum of intensity in $\text{H}\alpha$ image is one of the fundamental parameters. Applying a clipping allows us to increase the contrast of emission in the interarm region, thus improving the signal associated with the bar. But, on the other hand, if the trend found for the simulated bar applies for $\text{H}\alpha$ gaseous bar, the clipping we used for NGC 3367 could lead to an overestimation of the Ω_P by more than 50% and the bar would lie within a flat region of the curves shown in Fig. 8. Thus, if the clipping is not applied, our value of Ω_P indeed can be as small as $\sim 15 \text{ km s}^{-1}$. Yet, a deeper study using galaxy models with complex gas physics is required to verify whether the pattern speed is underestimated due to clipping. The other two parameters we investigated essentially restrain the range of integration parallel and perpendicular to the kinematic major

axis. These are underlying parameters that allow us to significantly improve the signal to noise ratio near the bar zone.

When observing the radial velocity field (Fig. 9), an interesting feature can be noted in the nuclear region. The isovelocity contours in the center of the galaxy that are almost perpendicular to the main ones may imply non-circular motions. Since the sharp turn in isophotes is frequently associated with a secondary bar, the possibility of non-circular motions due to different origins is present. In particular, the inner gas polar ring or disk, or a secondary bar may be responsible for the characteristic shape of the isovelocity contours. Such behavior has been observed previously in several galaxies, see for example Moiseev et al. (2004). However, due to lack of resolution, in this work we were unable to characterize and identify any secondary pattern speed. A study with a better angular resolution and a comparison with the stellar counterpart is necessary in order to analyze the detailed kinematical features in the center of this galaxy.

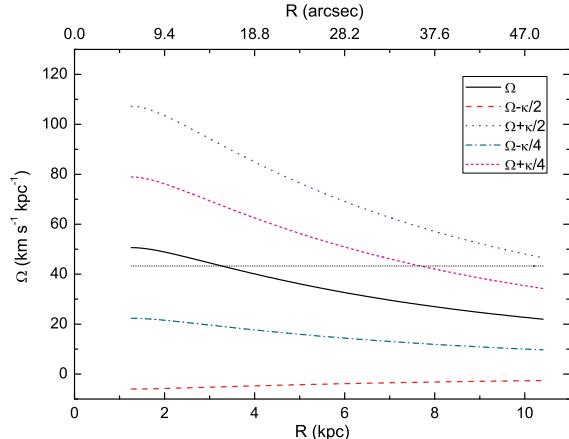


Fig. 16.— Resonances of NGC 3367. The dash-dotted horizontal line corresponds to the bar pattern speed, Ω_P , determined from the TW method.

6. Conclusions

In this work we apply the TW method to a simulated barred galaxy and test the sensitivity of the method to possible sources of error. Then we measure the bar pattern speed of NGC 3367 using the same method. The results obtained from the ap-

plication of this method to a simulated galaxy in general hold also for the observed one. However, the simulations have shown that a significant error can emerge due to applying the clipping to the surface density. These facts motivated us to assert some important conclusions within the limits of our work. First of all, bearing in mind the principal assumptions of the TW method, we can say that it works well enough for the gas phase whenever it is continuously distributed along the bar. On the other hand, the validity of applying clipping to the intensity map should be further investigated. We also want to note the importance of two dimensional data that allow the exploration of a wider range in parameters variation. Given the errors of the position angle determination the variation of $\delta PA \sim 5^\circ$ do not affect too much the resulting pattern speed for NGC 3367. Finally, determining the bar pattern speed by locating the corotation resonance, we found that the result is similar to that obtained by application of the TW method. This fact supports in part the reliability of the method in the case of ionized gas data. A deeper study of this galaxy would be worth, in particular, the comparison with the pattern speed determined from the stellar long-slit spectral observations, which would verify the validity of the TW method for H α kinematic data.

R.Gabbasov is supported by postdoctoral fellowship provided by UNAM. P.Repetto acknowledges CONACyT for doctoral scholarship. M.Rosado acknowledges CONACyT, project number 46054-F, and DGAPA, project number IN 100606. The simulations were performed on Kan-Balam computer at DGSCA, departament of supercomputing of UNAM.

REFERENCES

- Aguerri, J. A. L., Debattista, V. P., & Corsini, E. M. 2003, MNRAS, 338, 465
- Athanassoula, E. 2003, MNRAS, 341, 1179
- Beckman, J. E., Fathi, K., Piñol, N., Toonen, S., Hernandez, O., & Carignan, C. 2007, ArXiv e-prints, 07120518
- Canzian, B. 1993, ApJ, 414, 487
- Contopoulos, G. 1980, A&A, 81, 198

- Debattista, V. P. 2003, *MNRAS*, 342, 1194
- Debattista, V. P., Corsini, E. M., & Aguerri, J. A. L. 2002, *MNRAS*, 332, 65
- Debattista, V. P. & Williams, T. B. 2001, in *Astronomical Society of the Pacific Conference Series*, Vol. 230, *Galaxy Disks and Disk Galaxies*, ed. J. G. Funes & E. M. Corsini, 553–554
- Elmegreen, B. G., Elmegreen, D. M., Chromey, F. R., Hasselbacher, D. A., & Bissell, B. A. 1996, *AJ*, 111, 2233
- Elmegreen, B. G., Elmegreen, D. M., & Montenegro, L. 1992, *ApJS*, 79, 37
- Emsellem, E., Fathi, K., Wozniak, H., Ferruit, P., Mundell, C. G., & Schinnerer, E. 2006, *MNRAS*, 365, 367
- Fathi, K., Toonen, S., Falcón-Barroso, J., Beckman, J. E., Hernandez, O., Daigle, O., Carignan, C., & de Zeeuw, T. 2007, *ApJ*, 667, L137
- Fuentes-Carrera, I., Rosado, M., Amram, P., Dultzin-Hacyan, D., Cruz-González, I., Salo, H., Laurikainen, E., Bernal, A., Ambrocio-Cruz, P., & Le Coarer, E. 2004, *A&A*, 415, 451
- Fuentes-Carrera, I., Rosado, M., Amram, P., Salo, H., & Laurikainen, E. 2007, *A&A*, 466, 847
- Gabbasov, R. F., Rodríguez-Meza, M. A., Klapp, J., & Cervantes-Cota, J. L. 2006, *A&A*, 449, 1043
- García-Barreto, J. A., Franco, J., & Carrillo, R. 1996a, *ApJ*, 469, 138
- García-Barreto, J. A., Franco, J., Carrillo, R., Venegas, S., & Escalante-Ramírez, B. 1996b, *Rev. Mexicana Astron. Astrofis.*, 32, 89
- García-Barreto, J. A., Hernández-Toledo, H., Moreno-Díaz, E., Bernal-Marín, T., & Villarreal-Castillo, A. L. 2007, *AJ*, 134, 142
- García-Barreto, J. A. & Rosado, M. 2001, *AJ*, 121, 2540
- García-Barreto, J. A., Rudnick, L., Franco, J., & Martos, M. 1998, *AJ*, 116, 111
- Gerssen, J., Kuijken, K., & Merrifield, M. R. 1999, *MNRAS*, 306, 926
- Gioia, I. M., Maccacaro, T., Schild, R. E., Wolter, A., Stocke, J. T., Morris, S. L., & Henry, J. P. 1990, *ApJS*, 72, 567
- Hernandez, O., Carignan, C., & Amram, P. 2004, in *Astrophysics and Space Science Library*, Vol. 319, *Penetrating Bars Through Masks of Cosmic Dust*, ed. D. L. Block, I. Puerari, K. C. Freeman, R. Groess, & E. K. Block, 781
- Hernandez, O., Wozniak, H., Carignan, C., Amram, P., Chemin, L., & Daigle, O. 2005, *ApJ*, 632, 253
- Hernquist, L. 1990, *ApJ*, 356, 359
- . 1993, *ApJS*, 86, 389
- Kent, S. M. 1987, *AJ*, 93, 1062
- Kozintsev, B. & Kedem, B. 2000, *Journal of Computational and Graphical Statistics*, 9, 286
- Merrifield, M. R. & Kuijken, K. 1995, *MNRAS*, 274, 933
- Moiseev, A. V., Valdés, J. R., & Chavushyan, V. H. 2004, *A&A*, 421, 433
- Noguchi, M. 1987, *MNRAS*, 228, 635
- Rand, R. J. & Wallin, J. F. 2004, *ApJ*, 614, 142
- Rautiainen, P., Salo, H., & Laurikainen, E. 2005, *ApJ*, 631, L129
- Tremaine, S. & Weinberg, M. D. 1984, *ApJ*, 282, L5
- Tully, R. B. 1974, *ApJS*, 27, 449
- Westpfahl, D. J. 1998, *ApJS*, 115, 203
- Zimmer, P., Rand, R. J., & McGraw, J. T. 2004, *ApJ*, 607, 285

This 2-column preprint was prepared with the AAS L^AT_EX macros v5.2.